Physica Scripta

PAPER

RECEIVED
22 May 2025

REVISED
30 September 2025

ACCEPTED FOR PUBLICATION
24 October 2025

PUBLISHED
12 November 2025

Physio-chemical modification of CuSCN by lanthanum dopant towards improving hole transport mechanism for perovskite solar cell applications

Farah Liyana Rahim[1], Omsri Vinasha Aliyaselvam[1], Ahmad Shahiman Mohd Shah[2], A Shamsul Rahimi bin A Subki[1], Ahmad Nizamuddin Mustafa[1,3], Fauziyah Salehuddin[1], Merve Yakut[4,5] and Faiz Arith[1,*]

[1] Faculty of Electronics and Computer Technology and Engineering, Universiti Teknikal Malaysia Melaka, Hang Tuah Jaya, 76100, Durian Tunggal, Malaysia
[2] Department of Electrical Engineering, College of Engineering, Universiti Malaysia Pahang, Lebuhraya Tun Razak, Gambang, Pahang, Kuantan, 26300, Malaysia
[3] Department of Materials, Faculty of Engineering, Imperial College London, London SW7 2AZ, United Kingdom
[4] Department of Electrical and Electronics Engineering, Faculty of Engineering, University of Atatürk, Erzurum 25240, Türkiye
[5] School of Engineering, Newcastle University, Newcastle upon Tyne NE1 7RU, United Kingdom
[*] Author to whom any correspondence should be addressed.

E-mail: faiz.arith@utem.edu.my

Keywords: CuSCN, hole transport layer, perovskite solar cells, lanthanum

Abstract

Copper(I) thiocyanate (CuSCN) is gaining attention as an effective hole transport layer (HTL) in perovskite solar cells (PSCs) due to its excellent electronic properties, high stability, and superior hole mobility. Unlike the commonly used HTL Spiro-OMeTAD, which is sensitive to moisture and degrades quickly, CuSCN offers enhanced moisture resistance and improved durability without compromising efficiency. However, its low hole concentration and conductivity limit its performance. This study investigates the doping of CuSCN with lanthanum (La) to overcome these challenges. La doping introduces additional charge carriers, significantly increasing conductivity. Using dimethyl sulfoxide (DMSO) as a solvent for solution processing, we achieved a highly transparent and stable CuSCN HTL. The optimal La doping concentration was found to be 3 mol%, yielding a conductivity of 4.13 S cm^{-1} and a band gap of 3.67 eV. SCAPS-1D simulation analysis was further employed to optimize the CuSCN HTL thickness, identifying 100 nm as the ideal thickness to maximize device performance. With this thickness optimization, the power conversion efficiency (PCE) improved from 28.17% for pristine CuSCN to 30.54% with 3 mol% La doping. These results demonstrate that tailored La doping combined with optimized HTL thickness can effectively enhance CuSCN's properties, offering a promising route for developing high-performance and durable PSCs.

1. Introduction

Perovskite solar cells (PSCs) are the most promising contenders in thin-film photovoltaic technology [1]. With a dramatic increase in power conversion efficiency reaching over 31.16% in a short period, which is comparable to conventional silicon-based solar cells. This impressive progress is mainly due to the contribution of extensive research work on optimizing the composition of perovskite, device architecture, and interface engineering [2, 3]. The hole transport layer (HTL) is a key component in perovskite solar cells [4], facilitating efficient extraction and collection of photogenerated holes from the perovskite absorber layer to the metal electrode [5]. Furthermore, the HTL shields the perovskite film from environmental degradation, reduces charge recombination, and acts as a blocking layer to ensure highly efficient and stable solar cells [6]. HTLs are broadly categorized into organic and inorganic materials. Organic HTLs, such as spiro-OMeTAD [7]), PEDOT: PSS [7, 8], PTAA, and TPA [9–11], are widely used due to their excellent hole mobility and ease of processing.

However, these HTLs still face the issue of high cost and limited stability [12]. In contrast, inorganic HTLs, including copper oxides, nickel oxides [13], copper iodide [13, 14], copper thiocyanate [15–18], and copper selenocyanate [19, 20], offer superior chemical stability, high hole mobility, and exceptional optical transparency [21]. Furthermore, the synthesis of inorganic HTLs is simple and cost-effective, allowing them to be a viable alternative to organic HTLs.

Nickel oxide (NiO_x) is widely regarded as a promising hole transport layer (HTL) in perovskite solar cells due to its high stability and suitable energy alignment with perovskite absorbers. However, NiO_x has relatively low conductivity and surface defects that act as trap states, limiting performance and requiring improvement through surface passivation techniques (e.g., SAM interface layers) [22]. Additionally, the fabrication of NiOx often requires high-temperature annealing or vacuum-based processes, which may limit its compatibility with flexible or temperature-sensitive substrates [23]. In contrast, copper(I) thiocyanate (CuSCN) offers several advantages, including high hole mobility (0.01–0.1 $cm^2 V^{-1}{\cdot}s^{-1}$), a wide optical band gap (>3.5 eV), excellent stability against moisture and oxygen, and the ability to be deposited through simple, low-temperature, solution-processable methods [24]. Furthermore, CuSCN provides excellent thermal stability when used as a hole extraction layer, contributing to the overall stability of devices like perovskite solar cells [25]. These features make CuSCN an attractive alternative to NiO_x, particularly when combined with doping strategies to overcome its relatively low intrinsic conductivity. In this work, we explore lanthanum (La) doping of CuSCN to enhance its optoelectronic properties for stable and efficient PSC applications.

Lanthanum (La) doping of CuSCN emerges as a compelling strategy to augment its optoelectronic properties, thereby advancing the performance and stability of PSCs. La is selected as a dopant due to its demonstrated ability to enhance both the structural order and electronic quality of CuSCN. Specifically, trivalent La^{3+} ions effectively passivate intrinsic defects by suppressing deep trap states [26], which in turn mitigates nonradiative recombination losses at the CuSCN/perovskite heterointerface [27]. Moreover, the electropositive character and unoccupied 4 f orbitals of La^{3+} facilitate the formation of shallow acceptor states, leading to increased hole concentration and reduced electrical resistivity. Precedents in rare-earth doping, such as La incorporation in $BaSnO_3$ [28], have evidenced significant improvements in charge transport properties and energy band alignment within PSC devices, suggesting analogous benefits in CuSCN employed as a hole transport layer. Additionally, rare-earth elements, including La, are widely leveraged in inorganic semiconductors and catalytic materials for tuning electronic and optical functionalities, enhancing carrier mobility, and imparting enhanced long-term stability [29]. This study positions La doping as a strategic approach to optimize CuSCN-based hole transport layers for next-generation PSC technologies.

Along with its superior electronic properties, CuSCN has multiple versatile processing capabilities. Various solution processing methods are utilized to deposit CuSCN at relatively low temperatures, thus rendering it suitable for various applications in optoelectronic devices. These are spin-coating [17], ink-jet printing [30], doctor blading [31], and spray deposition [31]. The flexibility of these processing methods is expected to improve the manufacturability of devices and further pave the way for cost-effective production while maintaining high-quality film characteristics. Further improvements were made by developing a spray coating technique that minimized contact between the dipropyl sulfide solvent and the perovskite layer, resulting in an enhanced PCE of 17.1% [31]. Spin-coated methods were also used to deposit CuSCN in n-i-p PSCs, yielding efficiencies of 15.43% [32]. A significant challenge associated with the solution-processed method is identifying the ideal solvent to deposit CuSCN as the HTL due to its low solubility. Overall, the PCE with CuSCN HTL-based PSC is still less than 20%, further than the conventional PSCs.

Recent studies have highlighted physio-chemistry modification with various doping strategies for CuSCN to enhance cell efficiency and stability. The incorporation of tetrafluoro-tetracyanoquinodimethane (F_4TCNQ) as a dopant in CuSCN improves the hole transport mechanism and charge injection efficiency, leading to increased performance in perovskite solar cells and quantum dot light-emitting diodes [33]. Lithium (Li) increases hole mobility and crystallinity in overall perovskite solar cells, achieving efficiencies of over 20% [34]. Chlorine (Cl_2) doping enhances conductivity by orders of magnitude in p-CuSCN/n-GaN heterojunctions [35]. Additionally, fluorinated fullerene ($C_{60}F_{48}$) improves shunt resistance when used as a p-dopant in hole transport layers [36]. Overall, these dopants play crucial roles in optimizing the electrical properties of CuSCN HTLs.

Thereby, we investigate the impact of different doping concentrations of La in CuSCN as HTL and, ultimately, on the performance of the devices. In this work, different doping concentrations of La were varied utilizing a newly introduced high-polarity solvent, DMSO, for La-doped CuSCN synthesis. The grown La-doped CuSCN thin films were meticulously studied by field emission scanning electron microscopy (FESEM), x-ray diffraction (XRD), UV–vis, and I-V measurement.

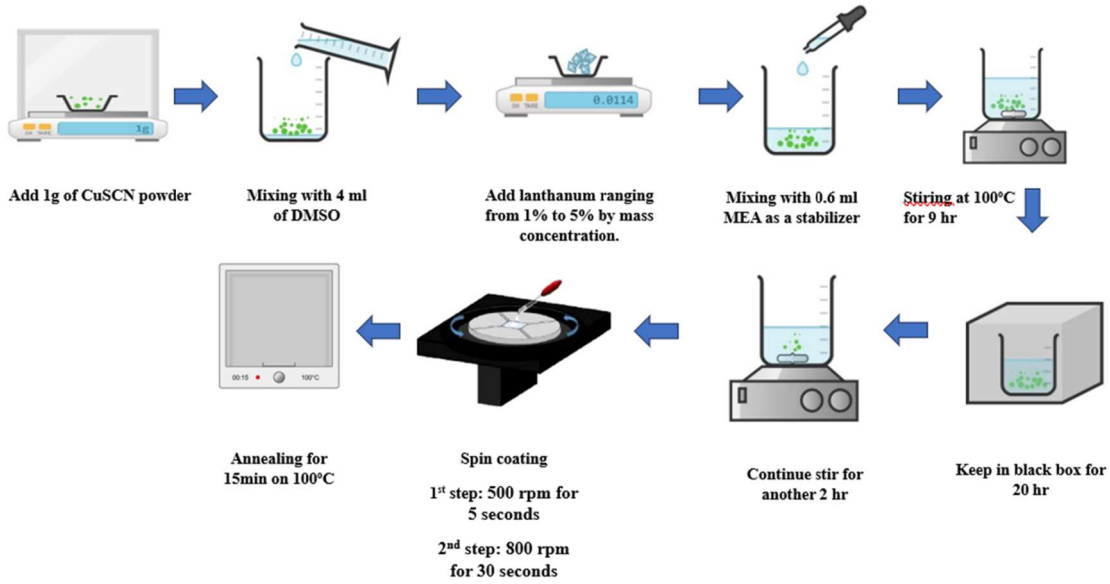

Figure 1. The schematic illustration of the La-doped CuSCN deposition process using the spin coating technique.

2. Materials and methods

2.1. Material and characterizations

Copper Thiocyanate (CuSCN) powders (99.999%), Lanthanum nitrate hydrate (99.99%), MEA (AR Grade, QReC), and dimethyl sulfoxide (DMSO) were acquired from Sigma-Aldrich. The surface morphology of the La-doped CuSCN films was observed using field emission scanning electron microscopy (FESEM; SU5000 from Hitachi). The grain size of both undoped and La-doped CuSCN films was determined by direct measurement from FESEM micrographs taken at a magnification of 10k×. The lateral dimensions of well-resolved grains were measured at multiple locations across different regions of the film surface to capture the variation in grain size. These measurements were averaged to provide a representative value of the average grain size, ensuring a statistically meaningful estimation of the grain size distribution. The crystal structure, orientation, and crystallite size of La-doped CuSCN were analyzed from x-ray diffraction (XRD) patterns obtained from PANalytical X'PERT PRO with CuKα radiation ($\lambda = 1.54056$ Å). The crystallite size, which refers to the dimension of individual coherent crystalline regions within a grain, was calculated from XRD data using the Scherrer equation in equation (4) [37]. Although the Williamson–Hall (W–H) method is also used to separate the contributions of crystallite size and lattice strain to peak broadening, the Scherrer equation was employed here for a straightforward estimation of crystallite size. X-ray photoelectron spectroscopy (XPS) was used to analyze the surface chemical composition and elemental states of the La-doped CuSCN films. Measurements were carried out with a monochromatic Al Kα source (h$\nu = 1486.6$ eV) under a base pressure of 5×10^{-8} bar. Optical properties in the CuSCN thin films were measured by the absorbance using a Shimadzu UV-1700 spectrophotometer. The charge carrier conduction mechanism was analyzed using a Keithley 2401 system, which was configured to perform a voltage sweep with a step size of 40 mV.

2.2. Sample preparation

The La-doped CuSCN solution was prepared by dissolving 1 g of CuSCN in 4 ml of DMSO, with 0.6 ml of MEA as a stabilizer as shown in figure 1 [38]. MEA likely coordinates with CuSCN, enhancing its solubility and preventing precipitation. DMSO was chosen for its ability to dissolve CuSCN and enable homogeneous incorporation of La dopants, which is challenging with low-boiling-point solvents [39]. The elevated temperature further promotes dissolution by increasing molecular motion and solvent–solute interactions [40]. Lanthanum was introduced into the solution at concentrations ranging from 1 to 5 mol%. The solution was vigorously stirred at 100 °C for 9 h. To prevent light-induced degradation, which can occur due to photochemical reactions of CuSCN under UV/visible light, resulting in copper species and impurities, the solution was stored in the dark for 20 h. Lanthanum salts are also sensitive to hydrolysis and particle agglomeration, which can be accelerated by light exposure. This dark storage step helps maintain the stability and reproducibility of the precursor, ensuring consistent film quality. After storage, the solution was re-stirred for an additional 2 h. The La-doped CuSCN solution was then carefully dripped onto the ITO glass substrate

Table 1. Input parameters of the pristine and La-doped CuSCN-based PSC.

Parameters	TiO_2 [42]	$MAPbI_3$ [44]	Pristine CuSCN [42]	La-doped CuSCN [42]
Layer thickness, d (μm)	0.025 (varies)	0.8 (varies)	0.1 (varies)	0.1 (varies)
Band gap energy, E_g (eV)	3.2	1.55	3.84 (experimental)	3.67 (experimental)
Electron affinity (eV)	3.9	3.9	2.1	2.1
Dielectric permittivity, ε (relative)	9.0	6.5	10	10
Conduction Band density of states, N_C (cm^{-3})	1×10^{19}	2.2×10^{18}	2.5×10^{18}	2.5×10^{18}
Valence Band density of states, N_V (cm^{-3})	1×10^{19}	2.2×10^{19}	1.8×10^{19}	1.8×10^{19}
Electron thermal velocity, V_e (cm/s)	1.0×10^{7}	1.0×10^{7}	1.0×10^{7}	1.0×10^{7}
Hole thermal velocity, V_h (cm/s)	1.0×10^{7}	1.0×10^{7}	1.0×10^{7}	1.0×10^{7}
Electron mobility, μ_e (cm^2/Vs)	2.0	2.0	2.0×10^{-4}	2.0×10^{-4}
Hole mobility, μ_p (cm^2/Vs)	1.0	2.0	1.0	1.0
Density of donor, N_D (cm^{-3})	1.0×10^{19}	NA	NA	NA
Density of acceptor, N_A (cm^{-3})	NA	1.0×10^{15}	1.0×10^{15}	1.0×10^{15}

Table 2. Input parameters of the interface layer of PSC.

Parameters	HTL/ Absorber [38]	Absorber/ETL [38]
Defect type	Neutral	Neutral
Capture cross-section electrons (cm^2)	1.0×10^{-19}	1.0×10^{-19}
Capture cross-section holes (cm^2)	1.0×10^{-19}	1.0×10^{-19}
Energetic distribution	Single	Single
Reference for defect energy level E_t	Above the highest E_V	Above the highest E_V
Energy with respect to reference (eV)	0.60	0.60
Total density (integrated over all energies) (cm^{-2})	1.0×10^{10}	1.0×10^{10}

and spin-coated using a two-step process at 500 rpm and 800 rpm for 5 s and 30 s, respectively. Finally, the film was annealed at 100 °C for 15 min.

2.3. PSC device simulation

The SCAPS-1D (Version 3.3.11) software provides a powerful platform for simulating perovskite solar cells (PSCs) incorporating La-doped CuSCN as the hole transport layer (HTL). Its calculations are based on steady-state solutions of the Poisson equation together with the continuity equations for electrons and holes, which collectively describe the electrostatic potential and charge-carrier dynamics within the device. The model accounts for key physical parameters, including the generation rate (G), electron and hole lifetimes (τ_n and τ_p), diffusion coefficient (D), electrostatic potential (Ψ), elementary charge (q), mobility of electrons and holes (μ_n and μ_p), concentrations of free (n(x), p(x),) and concentration of trapped electrons and hole ($n_t(x)$, $p_t(x)$); ionized acceptor and donor concentrations ($N_A^-(x) and N_D^+(x)$), electric field (ξ), and the spatial coordinate along the device thickness (x) [41]. By rigorously incorporating these parameters, SCAPS-1D enables a comprehensive description of charge transport, recombination, and electric-field distribution, thereby providing valuable insights into the optoelectronic performance of PSCs.

$$\frac{d}{dx}\left(-\varepsilon(x)\frac{d\varphi}{dx}\right) = q[p(x) - n(x) + N_D^+(x) - N_A^-(x) + p_t(x) - n_t(x)] \quad (1)$$

$$\frac{dp_n}{dt} = G_p - \frac{p_n - p_{n0}}{\tau_p} + p_n\mu_p\frac{d\xi}{dx} + \mu_p\xi\frac{dp_n}{dx} + D_p\frac{d^2p_n}{dx} \quad (2)$$

$$\frac{dn_p}{dt} = G_n - \frac{n_p - n_{p0}}{\tau_n} + n_p\mu_n\frac{d\xi}{dx} + \mu_n\xi\frac{do_n}{dx} + D_n\frac{d^2n_p}{dx} \quad (3)$$

A comprehensive PSC based on CuSCN was systematically modeled by integrating the experimentally derived optical properties of both pristine and 3 mol% La-doped CuSCN films. The key semiconductor parameters for the remaining functional layers are detailed in tables 1 and 2. Since experimental data on electron affinity and hole mobility for La-doped CuSCN are not yet available, the corresponding values for pristine CuSCN were adopted in simulations, consistent with previous CuSCN modeling studies [42]. A sensitivity analysis indicated that small variations in electron affinity (±0.1 eV) produced only marginal changes (<0.3% absolute) in PCE, while literature suggests that La doping induces minimal variation in hole mobility [36]. Therefore, a fixed mobility value was employed to retain model simplicity without compromising accuracy

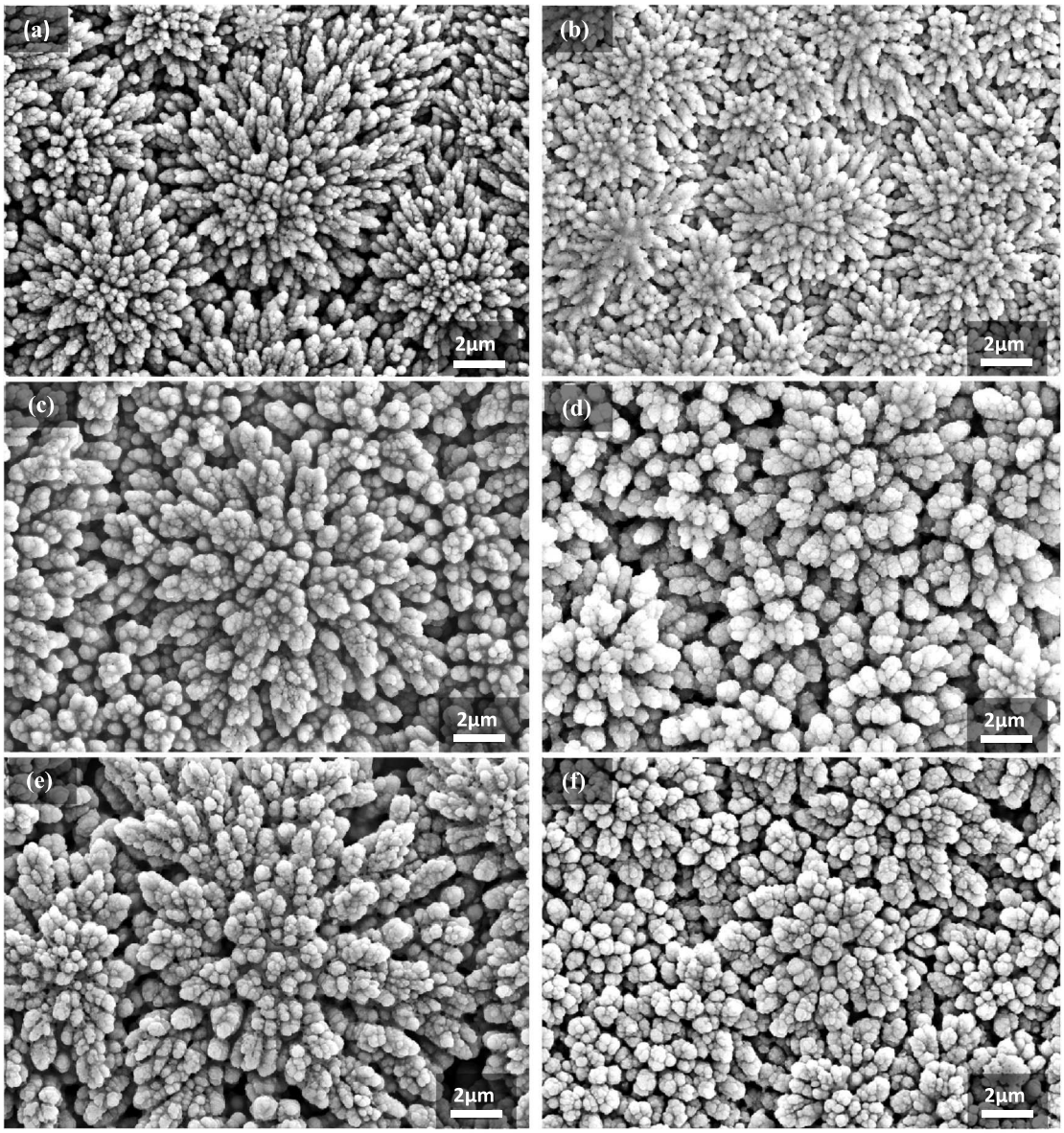

Figure 2. Top view FESEM images reef-like structure of La-doped CuSCN at different molar concentrations at ~3500 × magnifications, (a) 0 mol%, (b) 1 mol%, (c) 2 mol%, (d) 3 mol%, (e) 4 mol%, and (f) 5 mol%.

[43]. The device architecture consists of five principal layers: indium tin oxide (ITO) serving as the transparent conducting electrode, TiO_2 functioning as the electron transport layer (ETL), the perovskite absorber layer, pristine or La-doped CuSCN acting as the hole transport layer (HTL), and gold employed as the back contact. This structural design facilitates a direct comparative analysis of device performance between pristine and La-doped CuSCN within a fully operational PSC. The simulation studies utilizing SCAPS-1D were conducted under standardized illumination conditions, specifically employing AM1.5 G spectrum with an incident irradiance of 1000 W m^{-2}.

3. Results and discussion

3.1. Morphology analysis

The cross-sectional image (figure A.1) of the film reveals a thickness of approximately 3.7 μm. Although this is greater than that of conventional HTLs, previous studies have demonstrated that micrometer-scale CuSCN films can enhance film uniformity, improve hole transport properties, and provide mechanical robustness, thereby contributing to improved device stability and overall performance [45]. FESEM analysis (figure 2) reveals that all La-doped CuSCN layers developed reef-like nanostructures. Images of La-doped CuSCN films (0–5 mol% on ITO glass, ×~3500 magnification) indicate a distinct morphological evolution with increasing doping concentration. Figures 3(a)–(c) display patchy, reef-like morphologies with non-uniform coverage that

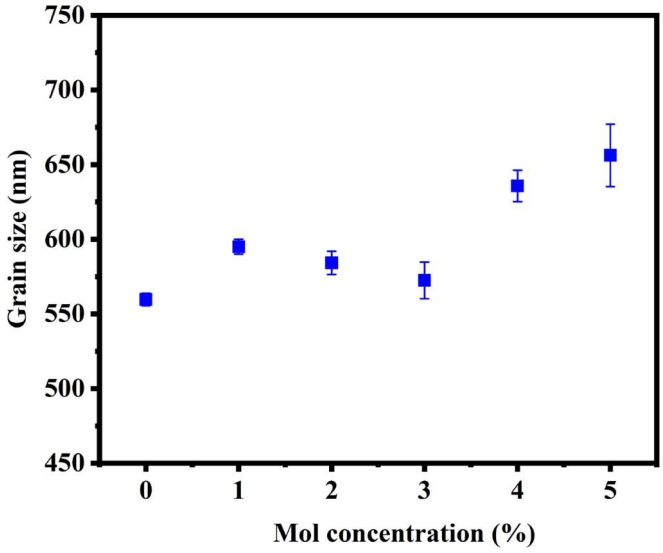

Figure 3. The grain size distribution for La-doped CuSCN at various molar concentrations of La.

exposes regions of the substrate, while radial spiky features emerge from nucleation centers. In contrast, figures 3(d)–(f) exhibit a more densely packed and homogeneous morphology, characterized by smaller surface features and reduced spiky characteristics. This transition indicates that higher La concentrations promote a shift from textured, reef-like structures to smoother and more compact arrangements.

Although the FESEM images suggest no drastic changes in the overall surface morphology with La doping, additional surface characteristics such as roughness and the aspect ratio of surface features, provide further insight. Measurements indicate that, despite the apparent morphological similarity, the aspect ratio improves with La incorporation, which is favorable for both charge transport and optical properties. Similar subtle influences of roughness and microstructure on device performance in CuSCN-based HTLs have been reported in the literature [46].

Porosity is another important aspect of the La-doped CuSCN HTL. A moderately porous HTL ensures sufficient interfacial area with the perovskite absorber layer, thereby facilitating efficient charge transfer. This porosity level provides a balance between enhanced interfacial adhesion and mechanical robustness, reducing the risk of delamination while maintaining efficient hole transport. The porosity level allows for adequate yet not excessive material absorption and release, contributing to device stability [47]. Furthermore, it offers a good compromise between mechanical stability and interfacial adhesion with the ETL, preventing delamination while maintaining efficient charge transport [47]. Typically, such porous nanostructures exhibit a moderate aspect ratio, where pores are noticeably longer than they are wide. These morphological evolutions underscore the critical role of La doping concentration in influencing the nanostructure formation and functional properties of CuSCN films.

In figure 3, the average grain sizes of the La-doped CuSCN samples were as follows: 585 nm for 1 mol%, 582 nm for 2 mol%, 592 nm for 3 mol%, 628 nm for 4 mol%, and 691 nm for 5 mol%. These variations in grain size possibly influence the performance of the material, as smaller grain sizes lead to an increased surface area, which is beneficial for photocatalysis due to the recombination rate suppressed by the electron–hole pairs [48]. The grain size of La-doped CuSCN tends to increase with the molar concentration of La doping increase due to several interconnected factors. Higher La concentrations promote enhanced nucleation and growth, resulting in larger crystal formation through the aggregation of smaller particles [49]. Additionally, the presence of La ions may induce lattice strain, which initially hinders growth but subsequently stabilizes larger particles. Furthermore, increased dopant concentration lowers the surface energy of the particles, allowing the merging of smaller grains into larger ones, which is thermodynamically favorable [49]. These effects contribute to the overall increase in grain size, a critical factor for optimizing hole transport properties in PSCs, where effective charge transport is essential for device performance.

3.2. Crystallography characterizations

Lanthanum (La^{3+}) and copper(I) (Cu^{+}) ions have almost similar ionic radii, which correspond to their various similar chemical characteristics. La^{3+} exhibits an ionic radius of 1.06 Å, compared to 0.96 Å for Cu^{+}, resulting in a size disparity of approximately 10%. In this context, the crystal structure of La-doped CuSCN was analyzed

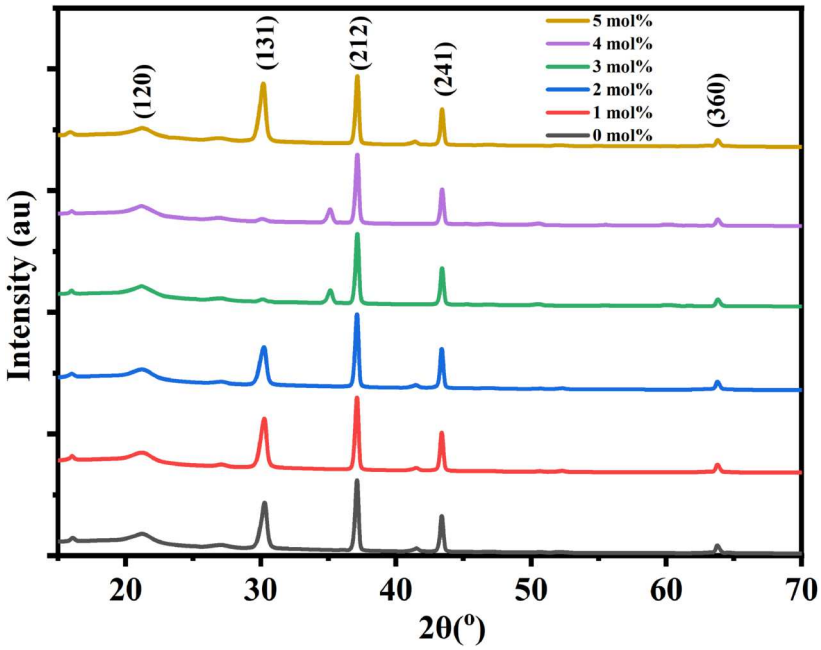

Figure 4. XRD pattern for variation molar concentration of La-doped CuSCN.

Table 3. The value of crystallite size and lattice constant for various La doping concentrations.

		Lattice constants (Å)		
La-doped CuSCN (mol%)	Crystallite Size, D (nm)	a	b	c
0	13.37	7.12	11.29	6.74
1	10.85	7.04	11.29	6.76
2	13.42	7.04	11.39	6.57
3	8.47	7.19	10.73	6.87
4	11.46	7.36	10.73	6.77
5	11.94	7.15	10.73	6.89

in detail using x-ray Diffraction (XRD) to uncover its crystallographic features, crystalline phases, chemical composition, and related physical properties [35, 36]. The average crystallite size of the La-doped CuSCN films was further estimated using the Scherrer equation equation (4), where K is the shape factor (0.9), D is defined as the crystallite size in nm, β is the full width at half maximum (FWHM) in degrees, λ is incident radiation wavelength ($\lambda = 1.5406$ Å) and θ is the Bragg's diffraction angle [50] . Based on the reflection $2\theta = 37.46°$, corresponding to the (2 1 2) plane, indicating the preferred orientation of the crystallites with the crystallographic *c*-axis perpendicular to the substrate. Four smaller peaks (figure 4) at $2\theta = 20.18°$, 30.30°, 43.30°, and 63.43° associated with (1 2 0), (1 3 1), (2 4 1), and (3 6 0) planes, respectively, were also identified. These peaks aligned with the α-phase of CuSCN, confirmed by comparing the experimentally measured 'd' values with the reference data provided in JCPDS card No. 00-029-0582 [51]. The absence of dominant (00 h) peaks suggests that the films are polycrystalline with mixed orientations, rather than exhibiting a strong preferential orientation strictly along the *c*-axis. This observation also indicates that La^{3+} substitution into the CuSCN lattice modifies the crystallinity without inducing a highly textured growth.

$$D = \frac{0.9\lambda}{\beta \cos\theta} \tag{4}$$

According to Bragg's law, shifts in diffraction peaks are directly related to changes in the d-spacing of the crystal lattice; specifically, an increase in d-spacing results in a shift of diffraction peaks to lower angles [52]. The peak positions and angles obtained from x-ray diffraction (XRD) spectra are instrumental in determining various structural parameters, including crystal sizes, d-spacing values, lattice constants, lattice strain, and dislocation densities [52, 53]. Concerning the variation of lattice parameters, La^{3+} ions are considered to substitute at

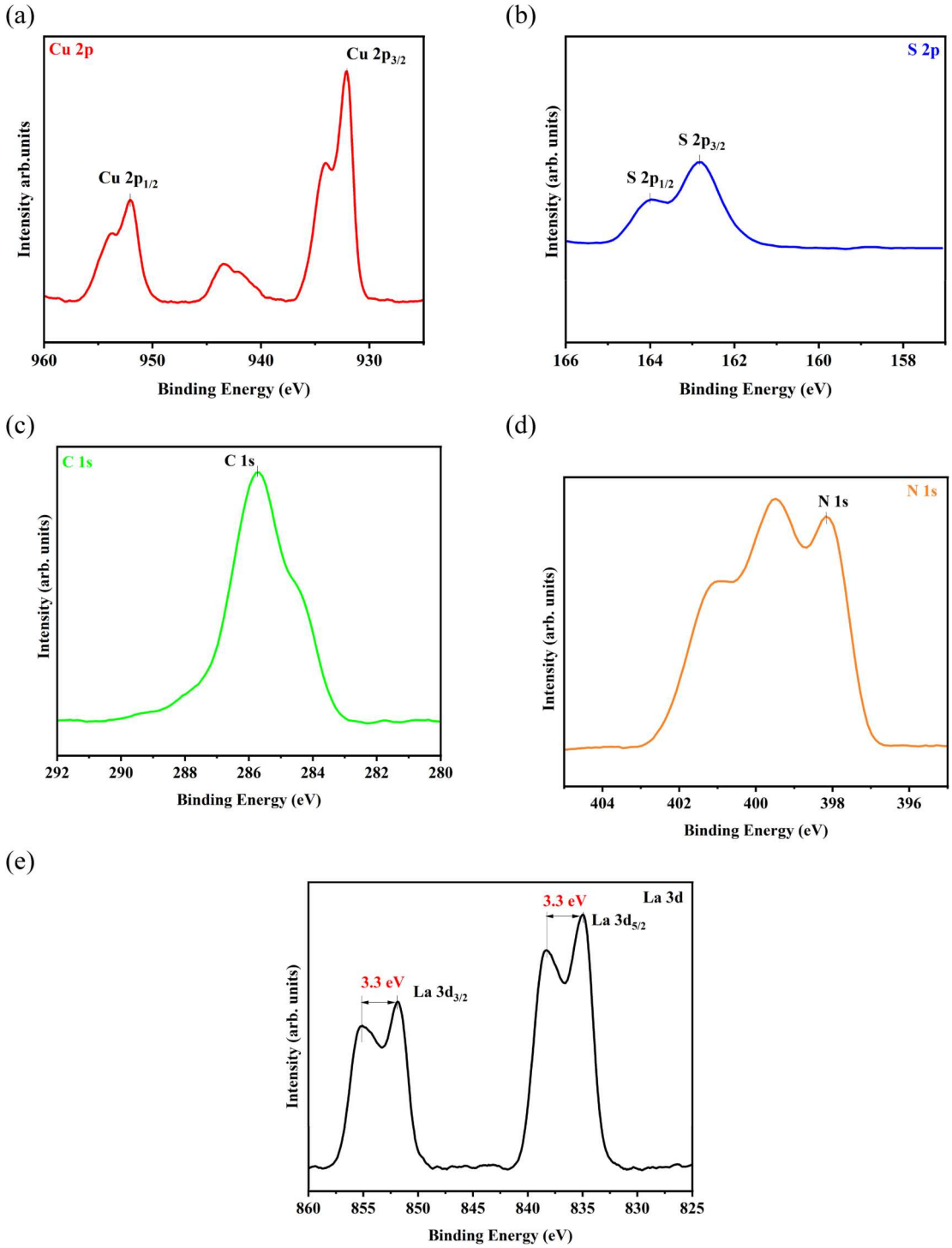

Figure 5. The XPS spectra of (a) Cu 2p, (b) S 2p (c) C 1 s (d) N 1 s (e) La regions of La-doped CuSCN films at 3 mol%.

the Cu^{+} sites within the CuSCN lattice. The non-linear change in lattice constants with increasing La concentration can be attributed to the significant ionic radius difference between La^{3+} (1.06 Å, CN = 6) and Cu^{+} (0.74 Å, CN = 6), which induces local lattice strain, together with the necessity of charge compensation arising from the trivalent state of La^{3+}, leading to the formation of defects such as Cu vacancies. These combined effects naturally cause deviations from the ideal Vegard's law linearity, while still supporting substitutional incorporation of La into the CuSCN lattice [54].

The crystallite size of La-doped CuSCN significantly influences its optical properties due to its impact on structural uniformity, defect density, and light interaction. In table 3, as the crystallite size decreases, the increased surface-to-volume ratio leads to a higher density of grain boundaries and defects, such as vacancies or interstitials, which introduce localized states in the bandgap. These defects often result in enhanced light

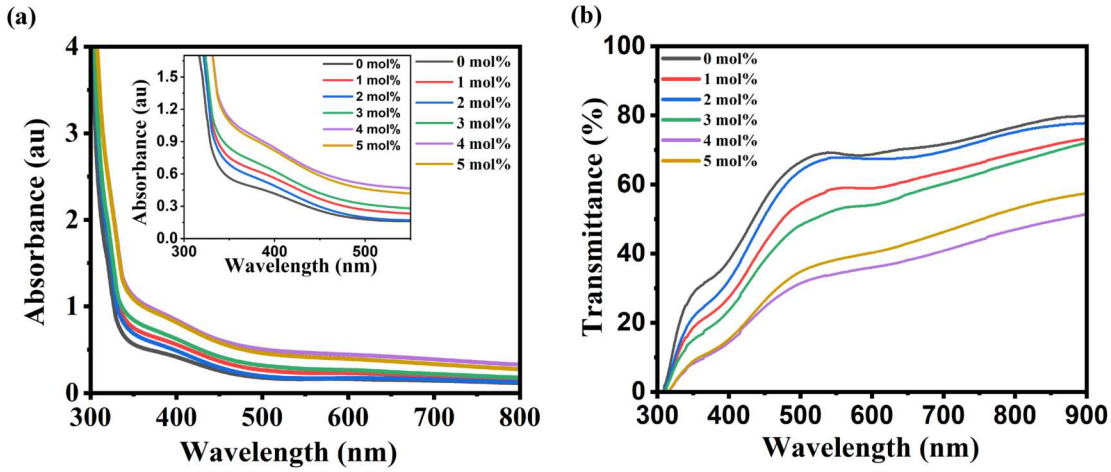

Figure 6. (a) Absorbance and (b) Transmittance spectra of CuSCN thin films with different molar concentrations of La.

scattering, reduced transparency, and altered photoluminescence characteristics [46]. Additionally, smaller crystallites possibly cause quantum confinement effects, subtly modifying the bandgap energy and optical absorption edge. As the value of La doping concentration increases, the crystallite size decreases, further amplifying these effects by reducing the overall crystallite dimensions and increasing the density of defects and grain boundaries.

3.3. Chemical state analysis

To clarify the chemical states and verify the effective incorporation of lanthanum into the CuSCN matrix, high-resolution x-ray photoelectron spectroscopy (XPS) was performed on the 3 mol% La-doped CuSCN sample. This specific doping level demonstrated superior electrical conductivity compared to other samples tested, highlighting its improved functional characteristics. The Cu 2p XPS spectra (figure 5(a)) of the La-doped CuSCN samples show that the binding energies of the Cu $2p_{3/2}$ and Cu $2p_{1/2}$ peaks remain largely consistent across all doping concentrations, at approximately 932 eV and 952 eV, respectively. These values align with those observed in pristine CuSCN [40], indicating that the copper chemical state (Cu^{+}) was preserved after lanthanum incorporation. The observed spin–orbit splitting of 20 eV corresponds well with the typical energy separation between Cu 2p core levels, further confirming that copper's oxidation state remains unchanged [55]. Nevertheless, an unusual peak appears near 942.94 eV, which may indicate interactions between lanthanum and the CuSCN matrix, possibly due to shake-up satellite features or new defect states. Despite this, the overall intensities and positions of the peaks remain similar to those of pristine CuSCN, suggesting that lanthanum doping does not significantly disrupt the copper environment but might induce subtle electronic effects at certain doping levels.

The S 2p region (figure 5(b)), the expected doublet at approximately 162 eV (S $2_{3/2}$) and ~164 eV (S $2p_{1/2}$), consistent with sulfur in the SCN^{-} ligand environment [40]. The C 1 s spectra (figure 5(c)) reveal a dominant peak near 285 eV, which corresponds to the C–N bond in the –SCN group of pristine CuSCN. A smaller shoulder observed in this region is attributed to aliphatic carbon (sp^3) impurities present on the film surface, commonly used as a calibration reference. Both pristine and La-doped samples exhibit this shoulder, ensuring reliable binding energy calibration. Figure 5(d) shows the N 1 s core-level spectra, where pristine CuSCN displays a characteristic peak around 398 eV [40], corresponding to nitrogen in the SCN^{-} group. An additional peak emerges near 401.06 eV in the La-doped sample, likely reflecting interactions with lanthanum. Despite these modifications, no new nitrogen species are detected, indicating that nitrogen remains mainly bonded as in the SCN^{-} group but with altered local electronic properties. In table 2, the pristine CuSCN data from the literature are compared with the 3 mol% La-doped CuSCN sample analyzed in this study. Table A.1 is the comparison of reported pristine and 3 mol of La-doped CuSCN.

The higher peaks of La $3d_{5/2}$ and La $3d_{3/2}$ in figure 4.6 are identified as satellite peaks [56]. The binding energies of La $3d_{5/2}$ and La $3d_{3/2}$ are measured at 834.94 eV and 851.89 eV, respectively. These satellites differ from the main peaks and are attributed to complex final-state phenomena such as multiplet splitting, shake-up processes, or plasmon loss effects. In lanthanum compounds, satellite peaks near the primary La 3d features have been reported, typically linked to electron correlation effects and charge transfer involving La 4f orbitals or interactions with surrounding ligands [57]. The spectra exhibit two prominent peaks that correspond to spin–orbit splitting of the La 3 d level into La $3d_{5/2}$ and La $3d_{3/2}$ components, which are typical for compounds

Table 4. The value of transmittance and band gap for various mol% of La doping concentrations.

La-doped CuSCN (mol%)	T (%) at 500 nm	Band gap (eV)
0	66.92	3.84
1	63.95	3.72
2	54.58	3.74
3	48.33	3.67
4	31.35	3.60
5	34.80	3.63

Table 5. The value of conductivity, resistivity and sheet resistance for various La doping concentrations.

La-doped CuSCN (mol%)	Conductivity (S cm^{-1})	Resistivity (Ω.cm)	Sheet resistance (kΩ sq^{-1})
0	3.36	0.30	9.91
1	3.04	0.33	11.0
2	2.19	0.46	15.2
3	4.13	0.24	8.07
4	4.52	0.22	7.38
5	3.90	0.26	8.55

containing lanthanum. The binding energies of La $3d_{5/2}$ and La $3d_{3/2}$ are reported to be approximately 835 eV and 852 eV, respectively [56]. This spin–orbit splitting results from the coupling between the electron's spin and orbital angular momentum, creating two discrete energy states for the 3d electrons. The measured splitting and relative peak intensities align well with the expected electronic structure of La^{3+} ions.

3.4. Optical performances

The optical quantum properties of La-doped CuSCN thin films deposited on ITO substrates were methodically analyzed to understand the light interaction with the solar spectrum. In figure 6(a), the outcomes imply that La-doped CuSCN exhibits a broad optical band, thus rendering the absorption degree low in the wavelength range of 500 to 800 nm [58]. However, the material demonstrates high UV absorption, particularly for wavelengths smaller than 500 nm. This unique characteristic shows the opportunity for La-doped CuSCN to conduct activities that require effective UV light absorption alongside transparency in the visible to near-infrared range, positioning it as a strong contender for various optoelectronic devices. In the context of La-doped CuSCN, increasing the doping concentration enhances the material's absorbance. This occurs because higher doping levels lead to an increased density of charge carriers, which facilitates more significant light absorption due to enhanced electronic transitions within the materials [59]. La doping possibly introduces additional energy levels within the bandgap, promoting electron transitions and improving light absorption [60]. The ionic radius of La^{3+} is larger than that of many other cations [61], resulting in lattice expansion and enhanced crystallinity [62]. By minimizing scattering losses, this structural alteration leads to a further increase in absorbance [34, 35].

The investigation of the transmittance (T) of La-doped CuSCN thin films, illustrated in figure 6(b), reveals a strong correlation between La concentration and the films' optical characteristics. The pristine CuSCN film shows a transmittance of 66.92% at 550 nm, which decreases substantially to 31.35% upon doping with 4 mol% La, before slightly increasing to 34.80% at 5 mol% La (table 4). This trend indicates that variations in doping concentration significantly influence the transmission values. Moreover, pristine CuSCN films experience a substantial decrease in transmittance from 66.92% to 31.35% at a wavelength of 550 nm upon introducing 4 mol% La (refer to figure 6(b) and table 4). This behavior suggests that variations in La doping significantly influence photon transmission, with the decline in transmittance at higher concentrations attributable to enhanced free-carrier absorption and dopant-induced scattering, consistent with previous studies on doped semiconductors [36–38]. The reduction in transparency is also associated with the introduction of localized electronic states and slight modifications in the band structure, leading to additional visible-light absorption [63]. While high transmittance is typically desired for hole transport layers, a moderate decrease would be advantageous for perovskite solar cell applications [64]. Specifically, doped CuSCN films reduce parasitic reflection, enhance light scattering into the perovskite absorber, and partially filter harmful UV radiation, thereby contributing to device stability [65]. More importantly, La doping improves hole mobility and

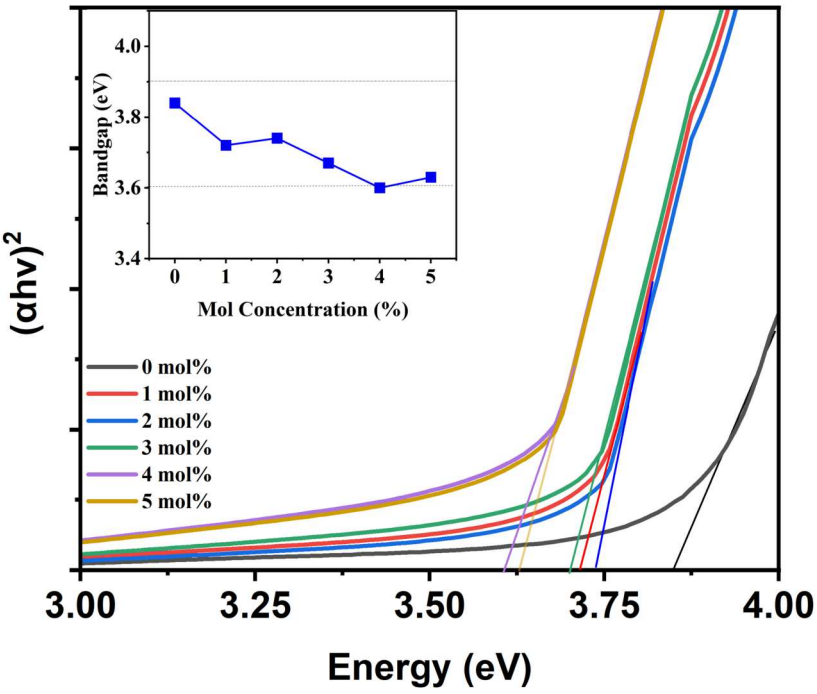

Figure 7. The tauc plot of La-doped CuSCN at different molar concentrations of La (inset: the band gap at various molar concentrations of La).

suppresses interfacial recombination, which compensates for the minor optical losses and results in an overall positive effect on device efficiency and operational stability [63].

Figure 7 shows the inset of the Tauc analysis employed to ascertain the optical bandgap (Eg) of CuSCN thin films based on their UV–vis absorption spectra. In this analysis, the quantity $(\alpha h\nu)^2$ was computed to evaluate the direct bandgap transition of photons as a function of photon energy ($h\nu$). In this equation, α represents the absorption coefficient, h denotes Planck's constant, and ν signifies the frequency of the incident radiation. This method is crucial for discovering the electronic properties of semiconductor materials, providing valuable insights into their potential applications in optoelectronic devices. The observed band gap energies for La-doped CuSCN at various doping concentrations (0–5 mol%) indicate a trend of decreasing energy levels, according to table 4. This reduction in band gap energy is attributed to the introduction of La atoms into the CuSCN lattice, which alters the electronic structure and enhances the material's optical properties.

Doping typically introduces new electronic states within the band gap, facilitating carrier mobility and potentially improving the semiconductor's performance in optoelectronic applications [66]. The band gap of pristine CuSCN was found to be 3.84 eV [67], suggesting that undoped CuSCN maintains its intrinsic properties. At the same time, subsequent doping leads to a progressive decrease in energy levels, indicating enhanced electron–hole pair generation under illumination [68]. This behavior aligns with findings in similar studies where doping elements modify the optical characteristics of semiconductors [69], confirming that La acts as an effective dopant in tuning the band gap of CuSCN for applications in solar cells and other optoelectronic devices [36, 40]. Moreover, the reduction of the band gap is attributable to the emergence of additional band tail states situated above the valence band edge, which may arise from structural deformation, as well as the presence of acceptor states introduced by dopants [70]. To quantify the band tail states, the Urbach energy (Eu) was extracted from the exponential absorption edge of the UV–vis spectra [71, 72]. The Eu values range from 0.280 to 0.310 eV across pristine and La-doped CuSCN films (0–5 mol%), showing minor fluctuations (average Eu = 0.294 ± 0.011 eV). This suggests that La incorporation slightly increases shallow tail states near the valence band, while the overall structural and optical quality of the films remains preserved.

3.5. Electrical performances

This study presents an approach to the characterization of La-doped CuSCN samples by utilizing the advanced capabilities of the Keithley-2401 digital source meter in a two-probe analysis mode. This methodology allows precise measurements of current and voltage but also facilitates a deeper exploration of the fundamental relationship between these two electrical parameters. Table 5 displays electrical conductivity, electrical resistivity, and sheet resistance with different doping concentrations. The results obtained are consistent with the above statement, as shown in figure 7. The value in figure 8 demonstrates that the resistance ranges from

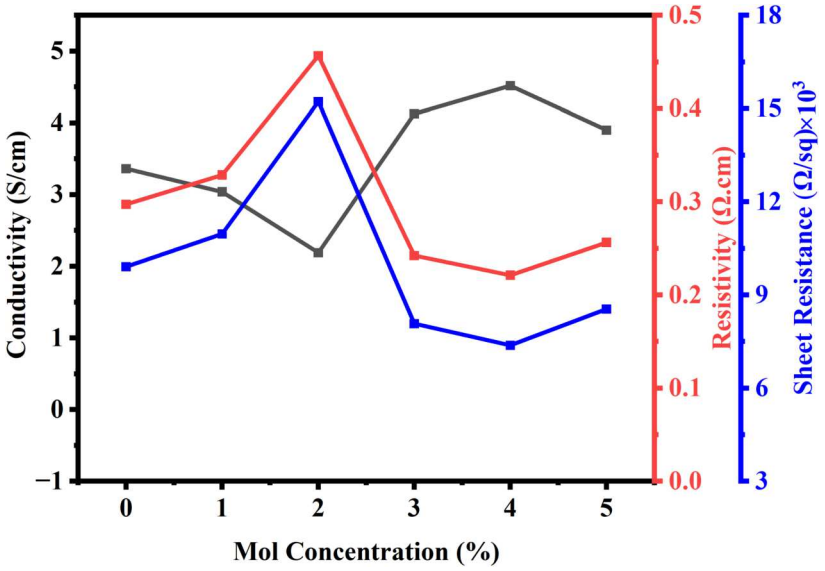

Figure 8. The electrical properties of La-doped CuSCN with various molar concentrations.

0.3 to 0.46 Ω cm; meanwhile, the conductance ranges from 2.19 to 4.52 S cm^{-1}. In this context, as nanoparticle size increases (refer to figure 3), the concentration of charge carriers (electrons and holes) typically increases, leading to enhanced conductivity. Larger nanoparticles have more atoms available on their surfaces, which contribute to higher charge carrier density [73]. The 4 mol% La-doped CuSCN exhibits the highest electrical conductivity at 4.52 S cm^{-1}, representing a significant increase of around 34% compared to pristine CuSCN.

$$\mathrm{Rs} = \frac{\rho}{\mathrm{t}} \tag{5}$$

Furthermore, the sheet resistance (Rs) of La-doped CuSCN varies significantly with different doping concentrations, reflecting the material's electrical properties. It is calculated using equation (4), where ρ represents the resistivity of the material and t is the thickness of the sample. The sheet resistance of La-doped CuSCN varies significantly with different doping concentrations, reflecting the material's electrical properties. The sheet resistance values for La-doped CuSCN indicate a clear trend in conductivity as doping levels change. At 2 mol% La doping, the peak sheet resistance is 15.2 kΩ sq^{-1}, which serves as a critical reference point for comparing other doping levels. In contrast, at 0 mol% La doping, the sheet resistance is lower at 9.91 kΩ sq^{-1}, suggesting better conductivity without any doping. As the doping concentration increases to 1 mol%, the sheet resistance rises to 11.0 kΩ sq^{-1}, reflecting a slight decrease in conductivity attributed to potential scattering effects. These findings highlight the impact of La doping on the electrical properties of CuSCN, indicating that while some doping enhances conductivity, excessive doping leads to increased resistance due to scattering mechanisms. As high electrical conductivity helps minimize the series resistance of the cell. However, conductivity alone is not enough to ensure optimal performance in solar cells. In many cases, the optical transmission in the visible spectrum is also crucial, as it enhances the photo-generated current, particularly those involving transparent conducting films [74]. To further highlight the significance of the obtained results, a comparison of the electrical and optical properties of La-doped CuSCN (this work) with commonly reported HTL materials is summarized in table 6. As shown, the conductivity of La-doped CuSCN (4.15 S cm^{-1}) is markedly higher than that of pristine CuSCN (0.6296 S cm^{-1}) and orders of magnitude higher than conventional HTLs such as NiOx (2.67×10^{-6} S cm^{-1}) and spiro-OMeTAD (2×10^{-4} S cm^{-1}). At the same time, the films retain an optical transmittance of approximately 60%, which is comparable to NiOx films deposited under certain conditions (~60%) [75] and spiro-OMeTAD (65%) [76]. This superior balance of high conductivity and reasonable optical transparency underscores the promise of La-doped CuSCN as a competitive HTL for PSCs.

3.6. Numerical simulation of complete device

The influence of HTL thickness was examined for the optimized 3 mol% La-doped CuSCN composition (figure 9), with the thickness varied between 100 and 1000 nm while keeping other parameters constant. The highest PCE of 30.68% was obtained at a thickness of 100 nm. As the HTL thickness increased from 100 to 1000 nm, the efficiency gradually decreased to approximately 30%, mainly due to a reduction in fill factor caused by increased series resistance [81]. Meanwhile, Voc remained nearly constant across the thickness range

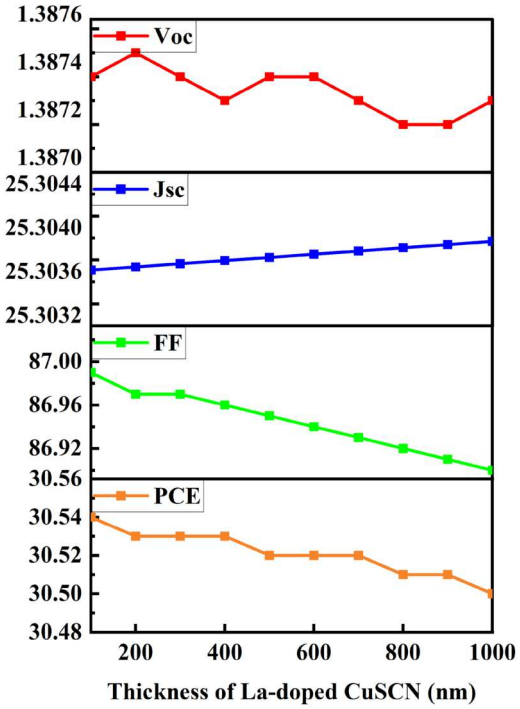

Figure 9. The variation of La-doped CuSCN thickness of simulated PSC for optimized 3 mol% La-doped CuSCN.

Table 6. Comparison of conductivity, resistivity, and transmittance of La-doped CuSCN with other reported HTMs (N/A = Not Available).

HTM	Conductivity (S cm^{-1})	Resistivity (Ω.cm)	Transmittance (%)
Pristine CuSCN [77]	6.296×10^{-1}	1.587	NR
NiO_x [78]	2.67×10^{-6}	3.74×10^{5}	85
NiOx 0.5 Pa [76]	N/A	N/A	~60
cp-NiO_x [79]	4.45×10^{-6}	2.25×10^{5}	NR
Spiro-OMeTAD [75]	N/A	N/A	>65
LiTFSI-doped Spiro-OMeTAD [80]	1.23×10^{-4}	8.13×10^{3}	N/A
Our Work (3 mol%)	4.15	0.241	~60%

because it is mainly determined by the absorber bandgap and recombination dynamics, which are not strongly affected by HTL thickness [82]. Since variations in the HTL do not alter the fundamental recombination pathways or bandgap of the absorber, Voc stability is expected [82].

In contrast, Jsc exhibited a slight increase with thickness, attributed to improved hole extraction and reduced interfacial recombination that outweighed the negligible optical losses in the wide-bandgap HTL [83], which minimizes transmission loss even at larger thicknesses [84]. Consequently, the photon flux reaching the absorber remains essentially unchanged [81]. The modest improvement in Jsc is attributed instead to enhanced hole extraction and reduced interfacial recombination losses in thicker HTLs, which compensate for any minor optical effects. It should be noted, however, that in practical devices, excessively thick HTLs may introduce measurable optical losses and reduce Jsc, an effect not fully captured within the present simulation framework.

The simulated J-V characteristics of complete devices employing pristine and La-doped CuSCN as HTLs are presented in figure 10. Both data in table 7 exhibit comparable short-circuit current densities (Jsc ~ 25 mA cm^{-2}), indicating that La incorporation does not compromise light absorption or charge generation in the perovskite layer. However, the La-doped CuSCN device demonstrates a superior power conversion efficiency (PCE) of 30.54%, representing an approximately 8% relative improvement over the pristine CuSCN device (28.17%). This enhancement is primarily attributed to improved hole extraction and transport resulting from the increased conductivity of La-doped CuSCN, which reduces series resistance and facilitates more efficient charge collection. In addition, La doping improves interfacial energy alignment at the perovskite/HTL interface, thereby suppressing non-radiative recombination and contributing to a higher open-circuit voltage (Voc). The sharper and more square-like J–V curve of the La-doped device also reflects a higher fill factor (FF),

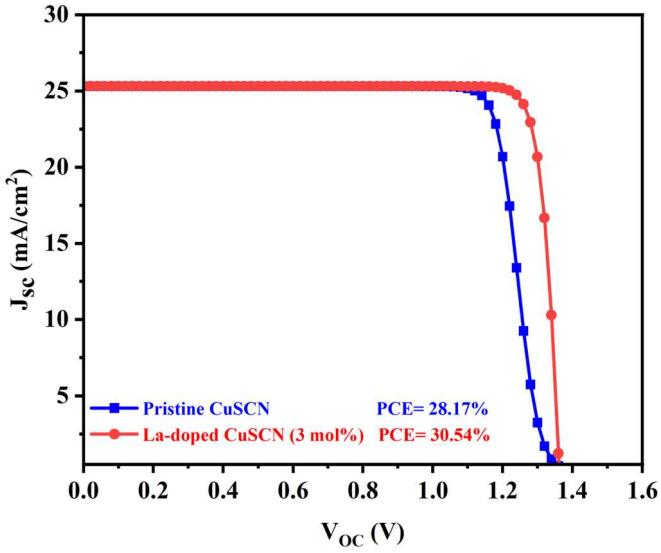

Figure 10. The J-V curve analysis for comparing pristine and La-doped CuSCN.

Table 7. Photovoltaic performance parameters of perovskite solar cells employing pristine CuSCN and 3 mol% La-doped CuSCN as the HTL, showing open-circuit voltage (Voc), short-circuit current density (Jsc), fill factor (FF), and power conversion efficiency (PCE).

Output Parameter	Pristine CuSCN	3 mol% La-doped CuSCN
Voc (V)	1.4622	1.3874
Jsc (mA cm^{-2})	25.3035	25.3035
FF	76.13	86.99
PCE (%)	28.17	30.54

confirming reduced resistive losses. Collectively, these results highlight the beneficial role of La doping in CuSCN toward achieving higher-efficiency and more stable perovskite solar cells.

4. Conclusions

In conclusion, the use of La-doped CuSCN as an HTL represents a significant advancement in the field of perovskite solar cells. Based on the factors studied, all elements, including morphology, microstructure, electron conduction mechanisms, crystallographic properties, and optical features, are undeniably interconnected. The structural performance of La-doped CuSCN films is analyzed using FESEM and x-ray Diffraction (XRD). Additionally, the electrical performance is assessed through current–voltage (I-V) characteristics, while the optical properties are scanned via UV–vis spectroscopy. Notably, under high magnification, the morphology of the CuSCN film doped with 5 mol% La reveals a distinct intercalated reef-like nanostructure characterized by well-defined grain edges that indicate complete growth. After a thorough analysis of the experimental results and various parameters measured, it has been determined that a concentration of 3 mol% yields one of the most favorable outcomes. This conclusion is based on a thorough evaluation of the data, which indicates that at this specific concentration, optimal performance was achieved. This specific concentration also demonstrates exceptional conductivity, reaching a notable value of 4.13 S cm^{-1}, and exhibits a bandgap of 3.67 eV, which is advantageous for applications requiring efficient charge transport and optical properties. Furthermore, the resistivity measurements indicate a low value, further underscoring the effectiveness of the 3 mol% composition in enhancing electrical performance. The crystallite size measured at 8.47 nm suggests a well-formed microstructure. The XPS analysis confirms the presence of all expected elements, Cu, S, C, N, and La, with La successfully incorporated at varying doping concentrations. Importantly, device performance tests show that the pristine CuSCN-based PSC achieves a PCE of 28.17%, while the 3 mol% La-doped CuSCN HTL further enhances the device efficiency to 30.54%, clearly

demonstrating the advantage of La incorporation. Moreover, the solution-processing method employed for the synthesis of La-doped CuSCN films at low temperatures underscores its practicality and cost-effectiveness, rendering it an attractive alternative for large-scale production. Overall, the 3 mol% La-doped CuSCN stands out as the most outstanding result regarding almost all the properties studied and its potential for efficient charge transport in perovskite solar cells, allowing it to be an attractive option for large-scale production.

Acknowledgments

This research is supported by a grant from the Royal Society of Chemistry, UK and Universiti Teknikal Malaysia, Melaka, under Grant ANTARABANGSA/RSC/2024/FKTEK/A00074.

Data availability statement

All data that support the findings of this study are included within the article (and any supplementary files).

Appendix

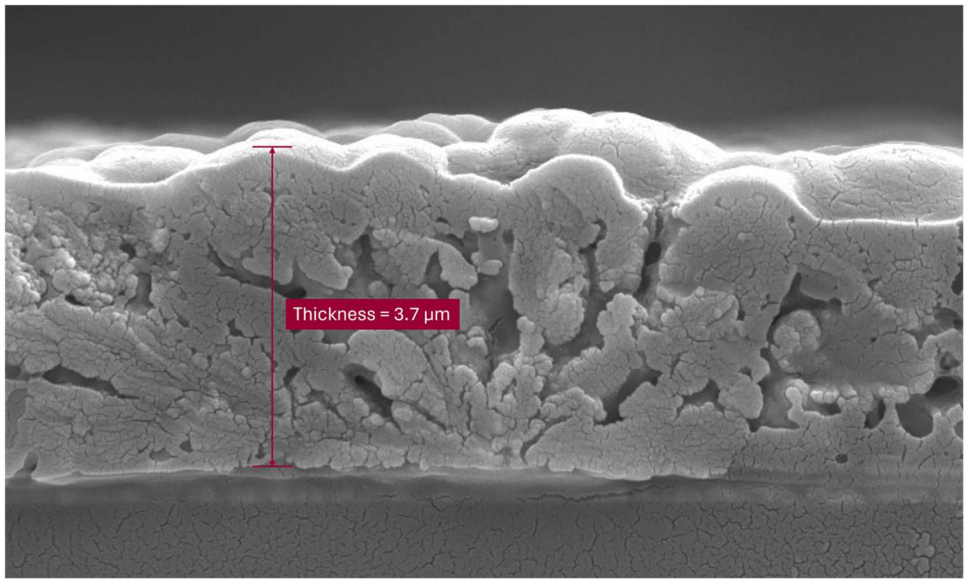

Figure A.1. The cross-sectional of the FESEM image.

Table A.1. Comparison of XPS core-level binding energies for pristine CuSCN reported and 3 mol% La-doped CuSCN films.

Core Level	Pristine CuSCN (eV) [40]	3 mol% (eV)
Cu $2p_{3/2}$	934.4	931.73
Cu $2p_{1/2}$	952.3	951.58
S $2p_{3/2}$	163.1	162.83
S $2p_{1/2}$	164.3	164.02
C 1 s	285.6	285.69
N 1 s	398.3	398.14

Author contributions

Farah Liyana Rahim 0009-0004-1879-3595
Data curation (equal), Formal analysis (equal), Investigation (equal), Writing – original draft (equal)

Omsri Vinasha Aliyaselvam 0000-0002-8748-1542
Conceptualization (equal), Data curation (equal), Validation (equal), Visualization (equal), Writing – review & editing (equal)

Ahmad Shahiman Mohd Shah 0000-0001-6387-4459
Methodology (equal), Software (equal), Supervision (equal), Validation (equal)

Merve Yakut 0009-0007-4588-0557
Conceptualization (equal), Methodology (equal), Validation (equal), Visualization (equal)

Faiz Arith 0000-0002-6459-8369
Conceptualization (equal), Data curation (equal), Formal analysis (equal), Project administration (equal), Resources (equal), Supervision (equal), Validation (equal), Visualization (equal), Writing – review & editing (equal)

References

[1] Rahim F L, Arith F, Izzati N, Jalaludin N, Salehuddin F, Shah A S and Mustafa A N 2024 Computational study of highly efficient SnO_2 ETL-based inorganic perovskite solar cell *Prz. Elektrotech.* **11** 99–103
[2] Shen G, Cai Q, Dong H, Wen X, Xu X and Mu C 2021 Using interfacial contact engineering to solve nickel oxide/perovskite interface contact issues in inverted perovskite solar cells *ACS Sustainable Chemistry and Engineering* **9** 3580–9
[3] Yang Z, Babu B H, Wu S, Liu T, Fang S, Xiong Z, Han L and Chen W 2020 Review on practical interface engineering of perovskite solar cells: from efficiency to stability *Solar Rapid Research Letter* (Wiley-VCH Verlag) https://doi.org/10.1002/solr.201900257
[4] Jalaludin N A, Salehuddin F, Rahim F, Mustafa A N, Kaharudin K E, Islam M A, Amin N and Arith F 2025 Efficient hole extraction by doped-polyaniline/graphene oxide in lead-free perovskite solar cell: a computational study *Phys. Scr.* **100** 025924
[5] Urieta-Mora J, García-Benito I, Molina-Ontoria A and Martín N 2018 Hole transporting materials for perovskite solar cells: a chemical approach *Chem. Soc. Rev.* (NLM (Medline)) https://doi.org/10.1039/c8cs00262b
[6] Bakr Z H, Wali Q, Fakharuddin A, Schmidt-Mende L, Brown T M and Jose R 2017 Advances in hole transport materials engineering for stable and efficient perovskite solar cells *Nano Energy* (Elsevier Ltd) https://doi.org/10.1016/j.nanoen.2017.02.025
[7] Mattiello S, Lucarelli G, Calascibetta A, Polastri L, Ghiglietti E, Podapangi S, Brown T, Sassi M and Beverina L 2022 Sustainable, efficient, and scalable preparation of pure and performing spiro-OMeTAD for perovskite solar cells *ACS Sustain Chem. Eng.* **10** 4750–7
[8] Han W, Ren G, Liu J, Bao H, Liu C and Guo W 2020 Recent progress of inverted perovskite solar cells with a modified PEDOT:PSS hole transport layer *ACS Appl. Mater. Interfaces* (American Chemical Society) https://doi.org/10.1021/acsami.0c13576
[9] Yi M, Jang W and Wang D H 2019 Controlled pH of PEDOT:PSS for reproducible efficiency in inverted perovskite solar cells: independent of active area and humidity *ACS Sustainable Chemistry and Engineering* **7** 8245–54
[10] Naqvi S and Patra A 2021 Hole transport materials for perovskite solar cells: a computational study *Mater. Chem. Phys.* **258** 123863
[11] Naqvi S, Yadav P, Pahari P and Patra A 2021 Dodecyl-substituted poly(3,4-ethylenedioxyselenophene): polymerization and its solution-processable applications for electrochromic and organic solar cells *J. Polym. Res.* **28** 250
[12] Naqvi S, Chaudhary N, Singhal S, Yadav P and Patra A 2021 Hole transport materials by direct C-H arylation for organic solar cells: effect of structure and conjugation on electrical, optical and computational properties *Chemistry Select* **6** 131–9
[13] Lee J H, Noh Y W, Jin I S, Park S H and Jung J W 2019 A solution-processed cobalt-doped nickel oxide for high efficiency inverted type perovskite solar cells *J. Power Sources* **412** 425–32
[14] Uthayaraj S, Karunarathne D, Kumara G, Murugathas T, Rasalingam S, Rajapakse R, Ravirajan P and Velauthapillai D 2019 Powder pressed cuprous iodide (CuI) as a hole transporting material for perovskite solar cells *J. Mater.* **12** 2037
[15] Chaudhary N, Kesari J P, Chaudhary R and Patra A 2016 Low band gap polymeric solar cells using solution-processable copper iodide as hole transporting layer *Opt. Mater.* **58** 116–20
[16] Chaudhary N, Chaudhary R, Kesari J P and Patra A 2017 An eco-friendly and inexpensive solvent for solution processable CuSCN as a hole transporting layer in organic solar cells *Opt. Mater.* **69** 367–71
[17] Chaudhary N, Chaudhary R, Kesari J P, Patra A and Chand S 2015 Copper thiocyanate (CuSCN): an efficient solution-processable hole transporting layer in organic solar cells *J. Mater. Chem. C* **3** 11886–92
[18] Chaudhary N, Naqvi S, Rathore D, Rathi S and Patra A 2022 Solvent influenced morphology control of hole transport layer of CuSCN on performance of organic solar cells *Mater. Chem. Phys.* **282** 125898
[19] Zhou Y, Liu C, Meng F, Zhang C, Wei G, Gao L and Ma T 2021 Recent progress in perovskite solar cells modified by sulfur compounds *Solar Rapid Research* (John Wiley and Sons Inc.) https://doi.org/10.1002/solr.202000713
[20] Bhargav R, Chaudhary N, Rathi S, Shahjad, Bhardwaj D, Gupta S and Patra A 2019 Copper bromide as an efficient solution-processable hole transport layer for organic solar cells effect of solvents *ACS Omega* **4** 6028–34
[21] Naqvi S, Chaudhary N, Kedia R, Yadav P and Patra A 2022 Copper (I) selenocyanate (CuSeCN): eco-friendly solution-processable deposition of hole transport layer for organic solar cells *Sol. Energy* **231** 496–502
[22] Alghamdi A R M, Yanagida M, Shirai Y, Andersson G G and Miyano K 2022 Surface passivation of sputtered NiOx using a SAM interface layer to enhance the performance of perovskite solar cells *ACS Omega* **7** 12147–57
[23] Shibayama N, Fukumoto S, Kanda H, Shioki T, Fukuda T, Oka Y, Haruyama Y, Suzuki S and Ito S 2024 Temperature dependence of spray pyrolysis NiOx layer in inverted perovskite solar cells *Oxford Open Energy* **3** oiae003

[24] Arora N, Dar M I, Hinderhofer A, Pellet N, Schreiber F, Zakeeruddin S M and Grätzel M 2017 Perovskite solar cells with CuSCN hole extraction layers yield stabilized efficiencies greater than 20%. *Science* **358** 768–71

[25] Odeke B A, Chung G D, Fajemisin J A, Suraj K S, Tonui D K, Tobi A R, Bewaale T C, Ajibola J A and Dzade N Y 2020 Electronic structure and surface properties of copper thiocyanate: a promising hole transport material for organic photovoltaic cells *Materials* **13** 1–14

[26] Aliyaselvam O V, Arith F, Mustafa A N, Chelvanathan P, Azam M A, Mahalingam M A and Amin. N 2025 Unveiling the prospect of copper iodide as hole transporting layer in perovskite solar cell by selective dopant strategy: a review *Mater. Sci. Semicond. Process.* **197** 109679

[27] Worakajit P, Kidkhunthod P, Thanasarnsurapong T, Waiprasoet S, Nakajima H, Sudyoadsuk T, Promarak V, Boonchun A and Pattanasattayavong P 2023 Origin of Hole-Trapping States in Solution-Processed Copper(I) Thiocyanate (CuSCN) and Defect-Healing by I_2 Doping *Advanced Functional Materials* **33** 2209504

[28] Myung C W, Lee G and Kim K S 2018 La-doped $BaSnO_3$ electron transport layer for perovskite solar cells *J. Mater. Chem. A* **6** 23071–23077

[29] Zainal Abidin N A, Arith F, Syahiman A, Ramadan S, Nizamuddin A, Safie N E, Azam M A, Rashid M and Chelvanathan P 2025 Compressive strain of La induced in ZnO nanorods by interstitial site passivation for enhanced charge carrier transport mechanism *Cryst. Growth Des.* **25** 4126–39

[30] Zhang X, Yoshioka S, Loew N and Ihara M 2014 Microstructure control of absorber S_2S_3 and p-type semiconductor CuSCN for semiconductor-sensitized solar cells (TiO_2 /S_2S_3 /CuSCN) *ECS Meeting Abstracts* **64** 1–13

[31] Yang I S, Sohn M I, Sung S D, Kim Y J, Yoo Y J, Kim J and Lee W I 2017 Formation of pristine CuSCN layer by spray deposition method for efficient perovskite solar cell with extended stability *Nano Energy* **32** 414–21

[32] Madhavan V E, Zimmermann I, Roldan-Carmona C, Grancini G, Buffiere M, Belaidi A and Nazeeruddin M K 2016 Copper thiocyanate inorganic hole-transporting material for high-efficiency perovskite solar cells *ACS Energy Lett.* **1** 1112–7

[33] Jin I S, Lee J H, Noh Y W, Park S H and Jung J W 2019 Molecular doping of CuSCN for hole transporting layers in inverted-type planar perovskite solar cells *Inorganic Chemistry Frontiers* **6** 2158–66

[34] Yang I S, Park Y J, Hwang Y, Yang H C, Kim J and Lee W I 2022 Formation of highly efficient perovskite solar cells by applying Li-doped CuSCN hole conductor and interface treatment *Nanomaterials* **12** 3969

[35] Liang J W *et al* 2022 Chlorine-infused wide-band gap p-CuSCN/n-GaN heterojunction ultraviolet-light photodetectors *ACS Appl. Mater. Interfaces* **14** 17889–98

[36] Wijeyasinghe N *et al* 2018 p-Doping of Copper(I) Thiocyanate (CuSCN) hole-transport layers for high-performance transistors and organic solar cells *Adv. Funct. Mater.* **28** 02055

[37] Islam M A, Rahaman M Z, Hasan M M and Hossain A K M A 2019 'Analysis of grain growth, structural and magnetic properties of Li-Ni-Zn ferrite under the influence of sintering temperature *Heliyon* **5** 1199

[38] Aliyaselvam O V, Arith F, Mustafa A N, Chelvanathan P, Azam M A and Amin N 2023 Incorporation of green solvent for low thermal budget flower-like Copper(I) Iodide (γ-CuI) for high-efficiency solar cell *J. Mater. Sci., Mater. Electron.* **34** 1274

[39] Wang B, Nam S, Limbu S, Kim J S, Riede M and Bradley D D C 2022 Properties and applications of Copper(I) thiocyanate hole-transport interlayers processed from different solvents *Adv. Electron. Mater.* **8** 2101253

[40] Jung S, Choi S, Shin W, Oh H, Kim N, Kim S, Kim N, Kim K and Lee H 2024 Effects of antisolvent treatment on Copper(I) thiocyanate hole transport layer in n-i-p perovskite solar cells *Molecules* **29** 4440

[41] Noorasid N S, Arith F, Salehuddin F, Mustafa A N, Chelvanathan P, Azam M A and Amin N 2023 Improved performance of lead-free Perovskite solar cell incorporated with TiO_2 ETL and CuI HTL using SCAPs *Appl Phys A Mater Sci Process* **129** 132

[42] Bhardwaj N, Ranjan R, Atul A K, Tiwari R N, Sharma A K and Srivastava N 2024 Numerical simulation study on the photovoltaic performance of tin-based perovskite solar cell using CuSCN as a hole transport layer giving 32% theoretical efficiency *Indian J. Phys.* **98** 1299–312

[43] Haider S.Z, Anwar H. and Wang M. Jun 2019 Theoretical Device Engineering for High-Performance Perovskite Solar Cells Using CuSCN as Hole Transport Material Boost the Efficiency Above 25% *Physica Status Solidi (A) Applications and Materials Science* **216** 11

[44] MallaHasan H and Onay Ö 2022 Investigation of the effect of different factors on the performance of several perovskite solar cells: a simulation study by SCAPS *European Journal of Engineering Science and Technology* **5** 20–38

[45] Sun J *et al* Additive engineering of the CuSCN hole transport layer for high-performance perovskite semitransparent solar cells *ACS Appl Mater Interfaces* **14** 52223–32

[46] Pattanasattayavong P, Promarak V and Anthopoulos T D 2017 Electronic properties of Copper(I) Thiocyanate (CuSCN) *Adv. Electron. Mater.* (Blackwell Publishing Ltd) https://doi.org/10.1002/aelm.201600378

[47] Li C and Gao P 2024 Crystalline porous materials in perovskite solar cells: a mutually beneficial marriage *Royal Society of Chemistry* **8** 1185–1207

[48] Nguyen L T T, Nguyen L T H, Duong A T T, Nguyen B D, Quang Hai N, Chu V H, Nguyen T D and Bach L G 2019 Preparation, characterization and photocatalytic activity of La-doped zinc oxide nanoparticles *Materials* **12** 1195

[49] Weng J H, Kao M C, Chen K H and Li M Z 2023 Influences of Cu doping on the microstructure, optical and resistance switching properties of zinc oxidethin films *Nanomaterials* **13** 2685

[50] Fatimah S, Ragadhita R, Fitria D, Husaeni A, Bayu A and Nandiyanto D 2021 How to Calculate Crystallite Size from X-Ray Diffraction (XRD) using Scherrer Method *ASEAN Journal of Science and Engineering* **2** 65–76 https://doi.org/10.17509/ajse.v2i1.37647

[51] Gates-Rector S and Blanton T 2019 The powder diffraction file: a quality materials characterization database *Powder Diffr.* **34** 352–60

[52] Bindu P and Thomas S 2014 Estimation of lattice strain in ZnO nanoparticles: x-ray peak profile analysis *Journal of Theoretical and Applied Physics* **8** 123–34

[53] Noorasid N S, Arith F, Aliyaselvam O V, Salehuddin F, Mustafa A N, Chelvanathan P, Azam M A and Amin N 2024 Low-temperature sol-gel synthesized TiO_2 with different titanium tetraisopropoxide (TTIP) molarity for flexible emerging solar cell *J. Sol-Gel Sci. Technol.* **109** 826–34

[54] Gonzalez Szwacki N, Fabrykiewicz P, Sosnowska I, Fauth F, Suard E and Przeniosło R 2023 Orthorhombic symmetry and anisotropic properties of rutile TiO_2 *J. Phys. Chem. C* **127** 19240–9

[55] Torres-Ochoa J A, Cabrera-German D, Cortazar-Martinez O, Bravo-Sanchez M, Gomez-Sosa G and Herrera-Gomez A 2023 Peak-fitting of Cu 2p photoemission spectra in Cu^0, Cu^{1+}, and Cu^{2+} oxides: a method for discriminating Cu^0 from Cu^{1+} *Appl. Surf. Sci.* **622** 156960

[56] Pui J, Zhou X, Pang Y, Zhu L, Vovk E I, Chong L, Alexander, Li S and Yang Y 2019 Understanding of binding energy calibration in XPS of lanthanum oxide by: *In situ* treatment *Phys. Chem. Chem. Phys.* **21** 22351–8

[57] Blanchard P E R, Slater B R, Cavell R G, Mar A and Grosvenor A P 2010 Electronic structure of lanthanum transition-metal oxyarsenides LaMAsO (M = Fe, Co, Ni) and LaFe1-xM′xAsO (M′ = Co, Ni) by x-ray photoelectron and absorption spectroscopy *Solid State Sci.* **12** 50–8
[58] Pattanasattayavong P, Yaacobi-Gross N, Zhao K, Ndjawa G O N D, Li J, Yang F, O'Regan B C, Ammasian A and Anthopoulos T D 2013 Hole-transporting transistors and circuits based on the transparent inorganic semiconductor copper(I) thiocyanate (CuSCN) processed from solution at room temperature *Adv. Mater.* **25** 1504–9
[59] Susilawati D A, Muhammad T, Syamsul H and Lalu M 2021 The optical properties of thin films tin oxide with triple doping (Aluminum, indium, and fluorine) for electronic device *Solid State Phenomena* (Trans Tech Publications Ltd) 477–82 https://doi.org/10.4028/www.scientific.net/SSP.317.477
[60] Karacaoglu E, Yildirim O A, Ozturk T and Gul M 2023 Effect of lanthanum doping on structural, optical, and photocatalytic properties of YVO_4 *J. Mater. Res.* **38** 3536–47
[61] Pandey A, Jain G, Vyas D, Irusta S and Sharma S 2017 Nonreducible, basic La_2O_3 to reducible, acidic La_2-xSbxO_3 with significant oxygen storage capacity, lower band gap, and effect on the catalytic activity *J. Phys. Chem. C* **121** 481–9
[62] Srivathsa M and Rajendra B V 2023 Effect of lanthanum doping on the structural, morphological, and optical properties of spray-coated ZnO thin films † *Engineering Proceedings* **59** 9032
[63] Gil B, Yun A J, Lee Y, Kim J, Lee B and Park B 2019 Recent progress in inorganic hole transport materials for efficient and stable perovskite solar cells *The Korean Institute of Metals and Materials* **15** 505–524
[64] Liu Y, Lin T, Huang R, Shi J and Chen S 2024 Analysis of the effect of copper doping on the optoelectronic properties of indium oxide thin films and the thermoelectric properties of an In_2O_3/Pt thermocouple *Crystals* **14** 0078
[65] Gu X, Li A, Rusli E, Xu X, Tao Z, Pan J, Yu X, Yu L and Mokkapati S 2024 An optical study on the enhanced light trapping performance of the perovskite solar cell using nanocone structure *Scientifics Reports* **14** 13363
[66] Lian J W *et al* 2022 Chlorine-infused wide-band gap p-CuSCN/n-GaN heterojunction ultraviolet-light photodetectors *ACS Appl. Mater. Interfaces* **14** 17889–98
[67] Waiprasoet S *et al* 2024 Doping of Copper(I) Thiocyanate (CuSCN) with metal chlorides for p-channel thin-film transistors *ACS Applied Electronic Materials* **9** 6837–6848
[68] Abdelfatah M, Darwesh N, Habib M A, Alduaij O K, El-Shaer A and Ismail W 2023 Enhancement of structural, optical and photoelectrochemical properties of n−Cu_2O thin films with K ions doping toward biosensor and solar cell applications *Nanomaterials* **13** 1272
[69] Rafique M, Khalid N R, Irshad M, Shafiq F, Usman M, Fouad Y, Imran M, Assiri M A and Ashraf W M 2023 Visible light-active pure and lanthanum-doped copper oxide nanostructures for photocatalytic degradation of methylene blue dye and hydrogen production *Energy Sci. Eng.* **11** 2601–13
[70] Kim M, Park S, Jeong J, Shin D, Kim J, Ryu S H, Kim K S, Lee H and Yi Y 2016 Band-tail transport of CuSCN: origin of hole extraction enhancement in organic photovoltaics *J. Phys. Chem. Lett.* **7** 2856–61
[71] Pandey A, Singh F, Garg A, Kanjilal D and Kumar L 2023 Work function modulation and charge transport studies of 100 MeV Au7+ ions irradiated TiO_2 films for optoelectronic devices *Opt Mater (Amst)* **143** 114180
[72] Al-Mahdi E A, Abdulwahab A M, Alnehia A, AL-Osta A and Al-Odayni A B 2025 Characterization of Zn-doped CuSCN Nano-powders synthesized via an *in situ* method for enhanced optical and structural properties *Results Chem* **14** 102140
[73] Abid H A and Al-Rashid S N T 2020 Study of the effect of nanoparticle size on the dielectric constant and concentration of charge carriers of Si and Cds materials *Chalcogenide Letters* **17** 623–9
[74] Mrabet C, Boukhachem A, Amlouk M and Manoubi T 2016 Improvement of the optoelectronic properties of tin oxide transparent conductive thin films through lanthanum doping *J. Alloys Compd.* **666** 392–405
[75] Islam M B, Yanagida M, Shirai Y, Nabetani Y and Miyano K 2017 NiO_x hole transport layer for perovskite solar cells with improved stability and reproducibility *ACS Omega* **2** 2291–9
[76] Khawaja K A, Xiang W, Wall J, Gu X, Li L and Yan F 2025 Hole transport layer selection for stable and efficient carbon electrode-based perovskite solar cells *RSC Adv.* **15** 13681–90
[77] Nizamuddin A, Arith F, Rong I J, Zaimi M, Rahimi A S and Saat S 2021 Investigation of Copper(I)Thiocyanate (CuSCN) as a hole transporting layer for perovskite solar cells application *Journal of Advanced Research in Fluid Mechanics and Thermal Sciences* **78** 153–9
[78] Kuo D W and Chen C T 2025 A dual layer of NiO_x hole-transporting material boosting the efficiency of inverted perovskite solar cells up to 20.7% *ACS Appl. Energy Mater.* **8** 5309–16
[79] Zhao K, Zhao Y, Tan Y, Hu K and Wang Z S 2021 Boosting the conductivity of the NiOx layer through cerium doping for efficient planar inverted perovskite solar cells *ACS Appl. Energy Mater.* **4** 9038–45
[80] Tabor D P, Chiykowski V A, Friederich P, Cao Y, Dvorak D J, Berlinguette C P and Aspuru-Guzik A 2019 Design rules for high mobility xanthene-based hole transport materials *Chem. Sci.* **10** 8360–6
[81] Saidani O, Goumri-Said S, Yousfi A, Sahoo G S and Kanoun M B 2025 Probing high-efficiency Cs0.05(FA0.77MA0.23)0.95Pb (I0.77Br0.23)3-based perovskite solar cells through first principles computations and SCAPS-1D simulation *RSC Adv.* **15** 7342–53
[82] Santos I M D L, Courel M, Moreni-Oliva V I, Duenas-Reyes E, Dian-Cruz E B, Ojeda-Martinez M, Perez L M and Laroze D 2025 The study of inorganic absorber layers in perovskite solar cells: the influence of CdTe and CIGS incorporation *Sci. Rep.* **15** 10353
[83] Reza M S *et al* 2025 A comprehensive investigation involving numerous HTL and ETL layers to design and simulate high-efficiency Ca_3AsI_3-based perovskite solar cells *Inorg. Chem. Commun.* **172** 113647
[84] Biswas S K, Sumon M S, Sarker K, Orthe M F and Ahmed M M 2023 A numerical approach to analysis of an environment-friendly Sn-based perovskite solar cell with SnO_2 buffer layer using SCAPS-1D *Adv. Mater. Sci. Eng.* **2023** 4154962